Interface Mismatch Relationship Between $YAlO_3$ and TiN: Insights From First- Principles

Weidong Ma[1,2,] Ligang Liu[2], Huixin Zheng[1], Xiaolei Xing[2], Yefei Zhou[2], Xuejun Ren[3], Jing Guo[4], Qingxiang Yang[1]

[1]State Key Laboratory of Metastable Materials Science & Technology, Hebei Key Lab for Optimizing Metal Product Technology and Performance, Yanshan University, Qinhuangdao, China.

[2]College of Mechanical Engineering, Yanshan University, Qinhuangdao, China.

[3]School of Engineering, Liverpool, John Moores University, Liverpool, UK,

[4]Department of Mechanical Engineering, Glasgow Caledonian University, Glasgow, UK

Abstract

The interface mismatch relationship between $YAlO_3$ and TiN was studied by first- principles calculation. The mismatch degrees between $YAlO_3$(001)//TiN(100) planes are the smallest (7.01%). It indicates that the hetero- nucleation effect of $YAlO_3$ on TiN is moderately effective. Four surface models were constructed for the $YAlO_3$(001) plane. Only one surface model was constructed for the TiN(100) plane. Six $YAlO_3$(001)//TiN(100) interface models were constructed. Among them, the interface adhesion work of O- N interface is the largest (8.11J/m^2). Meanwhile, the interface energy of O-N interface is the smallest (4.63 J/m^2). So, the O-N interface model is the most stable. The chemical bonds in this model are mainly the combination of Ti-O ionic bonds and N- O covalent bonds. Therefore, $YAlO_3$ meets the conditions to serve as the hetero nucleation core of TiN and tends to form an N-O terminated hetero nucleation interface.

1 Introduction

$YAlO_3$ represents an important material system in functional oxides [1, 2]. $YAlO_3$ has a hexagonal crystal structure. Due to its excellent chemical stability, wide optical band gap, and good lattice matching characteristics with various oxides, it is widely used as an epitaxial substrate material for high- temperature superconducting films, II- V nitride and oxide films [3, 4]. Titanium nitride (TiN) represents an important material system among transition metal nitrides [5, 6]. TiN has a NaCl- type face- centered cubic structure, and due to its extremely high hardness, excellent electrical conductivity, good thermal stability, and corrosion resistance, it plays a crucial role in wear- resistant coatings, diffusion barrier layers, as well as plasmon and nano- optical devices [7, 8].

Integrating TiN with $YAlO_3$ to form a heterojunction is expected to combine the functional characteristics of oxides (such as ferroelectricity, superconductivity, nonlinear optical response) with the metallic conductivity, high mechanical strength, and plasmonic properties of nitrides, thereby opening up an important path for the development of new multifunctional electronic and optical devices [9].

Currently, the heteroepitaxial integration of $YAlO_3$ and TiN faces a fundamental challenge—that there is a certain lattice mismatch between $YAlO_3$ and TiN. According to the traditional extrinsic growth theory, when the lattice mismatch is significant, it usually leads to the formation of high- density defects, three- dimensional island- like growth, and even poly- crystallization in the film, thereby seriously compromising the crystal quality and physical properties of the film [10, 11]. However, recent experimental studies have revealed an unexpected phenomenon: Despite the existence of certain lattice mismatch, high- quality single- crystal TiN films can still be obtained on $YAlO_3$

substrates by methods such as high- pressure magnetron sputtering [12]. What is more worthy of attention is that in the NbTiN/$YAlO_3$ system, the mismatched epitaxial films even outperform the similar films grown on the small- mismatch MgO substrates in terms of superconductivity and surface enhanced Raman scattering properties [13, 14]. These experimental findings indicate that the $YAlO_3$/TiN interface may possess a unique atomic- scale structural adaptation mechanism, enabling it to accommodate lattice mismatch without significantly compromising the quality of the epitaxial layer, which poses new challenges to the traditional theory of heteroepitaxy.

To understand this peculiar phenomenon at the atomic scale, it is necessary to systematically clarify the interface structure, bonding characteristics, and energy stability between $YAlO_3$ and TiN. In recent years, studies using transmission electron microscopy have revealed a rare interface overlapping structure between the rock salt structure TiN and the perovskite oxide $YAlO_3$, accompanied by periodic mismatch dislocations [15]. Meanwhile, the method combining the long-range lattice matching model with density functional theory has begun to be applied in the systematic study of complex heterogeneous interfaces, which can effectively evaluate the structural matching degree and energy stability of the interfaces [16]. However, the systematic first- principles studies on the $YAlO_3$/TiN interface are still relatively limited, especially in terms of the interface configuration, interface charge transfer, and bonding mechanism under different crystal orientation relationships, and there is still a lack of in- depth theoretical understanding in these aspects.

This study intends to employ the first- principles calculation method based on DFT (density functional theory), in conjunction with lattice mismatch analysis, to systematically investigate the interface issue between $YAlO_3$ and TiN. Firstly, by crystallographic analysis, the lattice mismatch degree of the two materials under different crystal planes and different orientation relationships is precisely calculated to determine the theoretically most stable interface matching mode. Secondly, a reasonable interface atomic model is constructed, and the equilibrium configuration of the interface is obtained by structural relaxation calculations. Then, the key physical quantities such as interface binding energy, interface energy, and electronic state density are calculated. Through these studies, the physical essence at the atomic scale of the $YAlO_3$/TiN interface is revealed, which can provide a theoretical basis for the rational design and experimental synthesis of nitride/oxide heterojunctions.

2. Computational Method

In order to optimize the bulk structures of $YAlO_3$ and TiN the VASP (Vienna Ab Initio Simulation Package) based on DFT was applied in this paper [17, 18] and the surface and interface properties of $YAlO_3$ and TiN were calculated. The GGA (generalized gradient approximation) functional improved by PBE (Perdew, Burke and Ernzerhof) was employed to calculate the exchange- correlation energy [19, 20].

The interaction between the ion nucleus and valence electrons was described by the PAW (projection augmented waves) [21]. The appropriate plane wave energy cutoff (Encut) and Brillouin zone Kpoint grid were selected by convergence tests.

The effect of Encut and K- points on the bulk phase of $YAlO_3$ and TiN was calculated. The Kpoints and Encut of $YAlO_3$ should be set to $8 \times 8 \times 8$ and 480 eV, respectively. The Kpoint and Encut of TiN should be set to 500 eV and $9 \times 9 \times 9$, respectively.

3 Results and Analysis

3.1 Crystal Structure and Bulk Properties

3.1.1 Crystal Structure

The crystal structures of $YAlO_3$ and TiN are shown in Figure 1. Figure 1a shows the crystal structure of $YAlO_3$. Its structure belongs to the hexagonal crystal system and the space group is P 63/mmc. The lattice constants are $a = b = 3.68 \neq c = 10.52$ Å, $\alpha = \beta = 90°$, $\gamma = 120°$. Figure 1b shows the crystal structure of TiN. Its structure belongs to the sodium chloride type, and its space group is FM- 3M. The lattice constants are $a=b=c= 4.416$ Å, $\alpha=\beta=\gamma= 90°$.

3.1.2 Bulk Properties

The bulk phase properties of $YAlO_3$ are shown in Figure 2. Figure 2a shows the energy band structure of $YAlO_3$. The position marked by the dotted line represents the Fermi level. It can be seen that there is a band gap of approximately 2.8 eV between the valence band and the conduction band of $YAlO_3$. Electrons can easily transition from the valence band to the conduction band, indicating that $YAlO_3$ has semiconductor properties. Figure 2b shows the density of states of $YAlO_3$. The dotted line position represents the Fermi level. In the range from −7 eV to the Fermi level, the peak intensity of the O-p orbital is higher than that of the Y- p and Y-d orbitals, indicating the formation of Y-O ionic bonds. Meanwhile, the peak intensity of the O- p orbital is also higher than that of the Al-s and Al-p orbitals, suggesting the formation of Al-O ionic bonds. Within the range of 3–7 eV, the Y-p orbital interacts with the O-p orbital, and the peak intensity of the Y-p orbital is higher than that of the O-p orbital, indicating the formation of Y-O ionic bonds. In conclusion, the chemical bonds in $YAlO_3$ are mainly Y- O ionic bonds and Al- O ionic bonds. The bulk phase properties of TiN have been reported by Reference [22].

3.2 Lattice Mismatch Degree Between YAlO3 and TiN

Bramfitt [21] proposed 2D lattice mismatch theory, in which, when the 2D lattice mismatch between the basal phase and the nucleating phase is less than 6%, the basal phase is able to play a very effective heterogeneous nucleation role with respect to the nucleating phase; with the mismatch degree of 6%–12%, the basal phase plays a moderately effective heterogeneous nucleation role with respect to the nucleating phase; and when the mismatch degree is larger than 12%, the basal phase cannot act as a heterogeneous nucleus for the nucleating phase. The two- dimensional lattice mismatch is calculated as follows [23]:

$$\delta_{(hkl)_n}^{(hkl)_s} = \sum_{i=1}^{3} \left[\left(\left| d_{[uvw]_s}^{i} \cos\theta - d_{[uvw]_n}^{i} \right| / d_{[uvw]_n}^{i} \right) / 3 \right] \times 100\% \quad (1)$$

where $(hkl)_s$ is a low- index crystal plane in the nucleation substrate; $[uvw]_s$ is a low- index crystal direction in the low- index crystal plane of the nucleation substrate; $(hkl)_n$ is a low-index crystal plane in the nucleation phase; $[uvw]_n$ is a low-index crystal direction in the low-index crystal plane of the

nucleation phase; $d_{[uvw]n}$ is the distance of atoms in the crystal plane of $(hkl)_n$ along the direction of $[uvw]_n$; $d_{[uvw]s}$ is the atomic distance along the $[uvw]_s$ direction in the $(hkl)_s$ crystal plane. θ is the angle between $[uvw]_n$ low- index crystal direction and $[uvw]_s$ low-index crystal direction.

Many low-index crystal planes of $YAlO_3$ and TiN were selected and their mismatch degrees were calculated, in which only the mismatch degrees of two low- index crystal planes of $YAlO_3$ and TiN are less than 12%. The results are listed in Table 1. From the calculated results, it can be seen that the mismatch degree of the $YAlO_3$(001) and TiN(100) planes is 7.01%, and that of the $YAlO_3$(001) and TiN(110) planes is 7.96%, whose values range from 6% to 12%, which indicates that the role of $YAlO_3$ as the hetero-nucleation core of TiN is moderately effective. Therefore, the $YAlO_3$(001) plane and TiN(100) plane with a smaller mismatch degree (7.01%) are selected to construct the surface and interface model.

3. Interface Properties

3.3.1 Surface Convergence Test

The surface models constructed for the $YAlO_3$(001) plane and TiN(100) plane were conducted for the surface energy convergence tests. The five surface models constructed are shown in Figure 3. There are four terminating surface models for $YALO_3$(001) plane, namely Y- terminated, O1- terminated, O2- terminated, and AlO-terminated surface models. Figure 3a–d shows three surface models of the $YAlO_3$ (001) plane. There is one surface model for the TiN(100) plane. Figure 3e depicts the surface model of TiN (100).

The $YAlO_3$(001) plane is a polar surface. The chemical potential calculation formula for the $YAlO_3$ surface model is as follows [24]:

$$\mu_{YAlO_3}^{bulk} = \mu_Y + \mu_{Al} + 3\mu_O \qquad (2)$$

where μ_{YAlO3}^{bulk} represents the energy of the system after the structural relaxation of $YAlO_3$ (001); μ_Y represents the chemical potential of the Y atom; μ_O represents the chemical potential of the O atom. The surface energy formula for calculating $YAlO_3$ (001) surface is as follows [24]:

$$\sigma_{YAlO_3(001)} = \frac{1}{2A}\left(E_{slab} - N_Y\mu_Y - N_O\mu_O - N_{Al}\mu_{Al}\right) \qquad (3)$$

where E_{slab} represents the energy value (J) of the surface model with a certain number of atomic layers; A represents the surface area of the model (m^2); N_Y represents the number of Y atoms in $YAlO_3$ (001) surface model; N_O represent the number of oxygen atoms in the $YAlO_3$ (001) surface model. For Y termination surface model, the calculation formula is as follows:

$$N_Y = N_{Al} + 2 \qquad (4)$$

For O1 termination surface model, the calculation formula is as follows:

$$N_Y = N_{Al} - 2 \quad (5)$$

$$N_O = 3N_{Al} \quad (6)$$

For O2 termination surface model, the calculation formula is as follows:

$$N_O = 3N_{Al} + 4 \quad (7)$$

For AlO termination surface model, the calculation formula is as follows:

$$N_O = 3N_{Al} - 4 \quad (8)$$

By combining Equations (2), (3) and (4) the final surface energy calculation formula for the Y surface model on the $YAlO_3(001)$

plane is as follows:

$$\sigma_{YAlO_3(001)} = \frac{1}{2A}\left[E_{slab} - N_{Al}\mu_{YAlO_3} - 2\mu_Y\right] \quad (9)$$

By combining Equations (2), (3) and (5), the final surface energy calculation formula for the O1 surface model on the $YAlO_3(001)$ plane is as follows:

$$\sigma_{YAlO_3(001)} = \frac{1}{2A}\left[E_{slab} - N_{Al}\mu_{YAlO_3} + 2\mu_Y\right] \quad (10)$$

By combining Equations (2), (3) and (7), the final surface energy calculation formula for the O_2 surface model on the $YAlO_3(001)$ plane is as follows:

$$\sigma_{YAlO_3(001)} = \frac{1}{2A}\left[E_{slab} - N_{Al}\mu_{YAlO_3} - 2\mu_Y - 4\mu_O\right] \quad (11)$$

By combining Equations (2), (3) and (8), the final surface energy calculation formula for the ALO surface model on the $YAlO_3(001)$ plane is as follows:

$$\sigma_{YAlO_3(001)} = \frac{1}{2A}\left[E_{slab} - N_{Al}\mu_{YAlO_3} - 2\mu_Y + 4\mu_O\right] \quad (12)$$

The $YAlO_3(001)$ surface energy calculated results of the three termination surfaces are listed in Table 2, Table 3, Table 4, and Table 5. As the number of surface layers increases, the fluctuation range of surface energy gradually becomes more stable. When the layer number of the Y terminated surface model exceeds 21, its surface energy stabilizes and converges to 2.06 J/m^2.

When the layer number of the O1 terminated surface model exceeds 19, its surface energy can stabilize and converge to 11.69 J/m2. When the layer number of the AlO terminated surface model exceeds 21, its surface energy stabilizes and converges to 10.76 J/m2.

For the $YAlO_3$(001) O2-terminated surface, we obtained a negative surface energy (−5.89–6.05 J/m^2). This unphysical value originates from the non-stoichiometric excess oxygen atoms on the surface, which undergo significant inward relaxation and form additional O–O interactions that artificially lower the slab energy relative to the reference state. A negative surface energy would violate thermodynamic stability (since it implies spontaneous cleavage), indicating that this ideal termination is not realizable. In experiment, such a surface would either desorb oxygen or reconstruct. Accordingly, we discarded this model and considered only terminations with positive surface energies for subsequent interface calculations.

The TiN (100) plane is a non-polar surface. The surface energy *TiN*(100) formula for calculating the TiN (100) surface is as follows [24]:

$$\sigma_{TiN(100)} = \frac{1}{2A}\left(E_{slab}^{N} - N\Delta E\right) \quad (13)$$

where E_{slab}^{N} represents the energy value (J) of the surface model with N atomic layers; E_{slab}^{N-2} represents the energy value (J) of the surface model with N-2 atomic layers; *A* represents the surface area of the model (m^2).

The TiN (100) plane is a non-polar surface, and the calculated surface energy results are listed in Table 6. As the number of surface layers increases, the fluctuation range of surface energy gradually becomes more stable. When the layer number of surface model reaches 9, the TiN (100) surface energy can be well converged to 1.34 J/m^2.

3.3.2 Interface Model

Depending on the different stacking methods, six $YAlO_3$(001)//TiN(100) interface models were constructed by selecting a 9-layer TiN (100) surface and respectively combining it with the Y-terminated surface of a 21-layer $YAlO_3$ (001), the O1-terminated surface of a 19-layer $YAlO_3$ (001), and the AlO-terminated surface of a 21-layer $YAlO_3$ (001), as shown in Figure 4. According to the different stacking methods, these six models were respectively named as Y-Ti, Y-N, O-Ti, O-N, AlO-Ti, and AlO-N interface models.

The energy variation curves of the six interface models with the interface spacing after relaxation are shown in Figure 5. It can be seen that for the Y-Ti interface model, the energy is the lowest when the interface spacing is 2.6 A; for the Y-N interface model, the energy is the lowest when the interface spacing is 2.2 A; for the O-Ti and O-N interface models, the energy is the lowest when the interface spacing is 1.6 A; for the AlO-Ti and AlO-N interface models, the energy is the lowest when the interface spacing is 2.4 A.

3.3.3 Interface Adhesive Work and Interface Energy

The interface adhesive work (*W*ad) is an important parameter for characterizing the strength of the interface bonding. For the interface model of $YAlO_3$(001)//TiN(100), the calculation formula for *W*ad is as follows [25]:

$$W_{ad} = \frac{1}{A}\left(E_{YAlO_3} + E_{TiN} - E_{YAlO_3/TiN}\right) \quad (14)$$

where $E_{YAlO3/TiN}$ represents the energy value (J) of $YAlO_3$(001)//TiN(100) interface model; E_{YAlO3} represents the energy (J) of $YAlO_3$ (001) surface model; E_{TiN} represents the energy (J) of TiN (100) surface model; A represents the interface area (m^2).

The interface energy (γ) corresponds to the difficulty of heterogeneous nucleation at the interface. The calculation formulas for γ of the four interface models are as follows [23]:

$$\gamma = \sigma_{YAlO_3} + \sigma_{TiN} - W_{ad} \quad (15)$$

where σ_{YAlO3} represents the surface energy (J/m^2) of the $YAlO_3$ (001) surface model; σ_{TiN} represents the surface energy (J/m^2) of the TiN (100) surface model.

The *Wad* and *γ* values of the six YAlO3(001)//TiN(100) interface models are shown in Figure 6. The W_{ad} sequence of the six interface models is as follows: $W_{adO\text{-}N} > W_{adO\text{-}Ti} > W_{adY\text{-}Ti} > W_{adY\text{-}N} > W_{adAlO\text{-}N} > W_{adAlO\text{-}Ti}$.

The *γ* sequence of the six interface models is as follows: $\gamma_{O\text{-}N} < \gamma_{O\text{-}Ti} < \gamma_{Y\text{-}Ti} < \gamma_{Y\text{-}N} < \gamma_{AlO\text{-}N} < \gamma_{AlO\text{-}Ti}$.

It can be seen that both the O-terminated surface of $YAlO_3$(001) and the interface model on the TiN(100) surface are relatively stable. Among them, the W_{ad} value of the O-N interface is the largest, which is 8.11 J/m^2. Meanwhile, the γ value of the O-N interface is the smallest, which is 4.63 J/m^2. Therefore, the O-N interface is the most stable.

3.3.4 | Interface Model Bonding Characteristics

By calculating the charge density and differential charge density of the $YAlO_3$(001)//TiN(100) interface model, the bonding characteristics of the $YAlO_3$(001)//TiN(100) interface model are analyzed, and the stability of the interface is further determined.

The charge densities of the (100) section of six $YAlO_3$(001)//TiN(100) interface models are shown in Figure 7. In this figure, the charge accumulation areas are indicated by the red regions, and the charge depletion areas are indicated by the blue regions. The color changes from blue to red to represent the increasing charge density. Figure 7a shows the charge density of the Y-Ti interface in $YAlO_3$(001)//TiN(100) interface model. Figure 7b shows the charge density of the Y-N interface in $YAlO_3$(001)//TiN(100) interface model. It can be seen that the atomic distances at the interfaces are relatively far apart, making it difficult for bonding to occur. Figure 7c shows the charge density of the O-Ti interface in $YAlO_3$(001)//TiN(100) interface model. It can be concluded that during the relaxation process, Ti atoms diffuse downward while O atoms diffuse upward. There are numerous charge accumulation areas around the O atoms, indicating that the charge density around the O atoms is high and the O atoms gain electrons.

There are also numerous charge depletion areas around the Ti atoms, indicating that the charge density around the Ti atoms is low and the Ti atoms lose electrons. Figure 7d shows the charge density of the O-Ti interface in $YAlO_3$(001)//TiN(100) interface model. It can be observed that during the relaxation process, the N atoms diffuse downward while the O atoms diffuse upward, and there is an overlapping area of charges for the two types of atoms, indicating the formation of chemical bonds between the

two types of atoms. Figure 7e shows the charge density of the AlO-Ti interface in $YAlO_3$(001)//TiN(100) interface model. Figure 7f shows the charge density of the AlO-N interface in $YAlO_3$(001)//TiN(100) interface model. Due to the large distance between the atoms at the interface, it is difficult for chemical bonds to form.

The formula for calculating the differential charge density is as follows [23]:

$$\rho_d = \rho_{tot} - \rho_{YAlO_3} - \rho_{TiN} \quad (16)$$

where ρ_{tot} represents the total charge density in the interface model; ρ_{YALO3} represents the charge density of the individual YAlO3(001) plane within the same interface model; ρ_{TiN} represents the charge density of the individual TiN(100) plane within the same interface model.

As can be seen from Figure 7, only the O-Ti and O-N interfaces in the $YAlO_3$(001)//TiN(100) interface model can form bonds. Only the differential charge densities of the O-Ti and O-N interfaces in the $YAlO_3$(001)//TiN(100) interface model were calculated in this paper, as shown in Figure 8. The charge accumulation areas are indicated by the red regions, and the charge depletion areas by the blue regions. The color ranges from blue to red to represent the increasing charge density. Figure 8a shows the differential charge density at the O-Ti interface in the $YAlO_3$(001)//TiN(100) interface model. It can be seen that the charge density around the O atom is relatively high, while that around the Ti atom is relatively low. Thus, a Ti-O ionic bond is formed between them.

Figure 8b shows the differential charge density at the O-N interface in the $YAlO_3$(001)//TiN(100) interface model. It can be seen that simultaneously around the N atom and the O atom, there are regions of charge accumulation and regions of charge depletion, and an N-O covalent bond is formed between them.

4 Conclusion

1. The minimum mismatch degree between the $YAlO_3$ (001) plane and TiN (100) plane is 7.01%, indicating that the heterogeneous nucleation effect of $YAlO_3$ on TiN is moderately effective.

2. The surface models of $YAlO_3$ (001) and TiN (100) were selected to conduct surface energy convergence tests. It was found that when the layer number exceeds 21, the surface energy of the Y-terminated surface model on the $YAlO_3$(001) plane can converge to 2.06 J/m^2; when the layer number exceeds 19, the surface energy of the O1-terminated surface model on the $YAlO_3$(001) plane is 11.69 J/m^2; since the surface energy of the O2-terminated surface model on the $YAlO_3$(001) plane is negative, it indicates that this model is unstable; when the layer number exceeds 21, the surface energy of the AlO-terminated surface model on the $YAlO_3$(001) plane converges to 10.76 J/m^2. When the number of layers of the TiN (100) surface model reached 9, the surface energy converged to 2.75 J/m^2.

3. The interfacial adhesion work and interfacial energy of four $YAlO_3$(001)//TiN(100) interface models were calculated. Among them, the interfacial adhesion work of the O-N interface is the largest, which is 8.11 J/m^2. Meanwhile, the interfacial energy of the O-N interface is the smallest, which is 4.63 J/m^2. Therefore, the O-N interface model is the most stable.

4. The chemical bonds in this model are mainly the combination of Ti-O ionic bonds and N-O covalent bonds.

Author Contributions :Weidong Ma: conceptualization, methodology, investigation, writing–original draft. **Ligang Liu**: methodology, resources. **Huixin Zheng**: data curation, visualization. **Xiaolei Xing**: methodology, resources. **Yefei Zhou**: methodology, resources. **Xuejun Ren**: resources, project administration, funding acquisition. **Jing Guo:** methodology. **Qingxiang Yang:** conceptualization, investigation, methodology, resources, software, funding acquisition, writing – review and editing, supervision.

Acknowledgments

The authors would like to express their gratitude for projects supported by the National Natural Science Foundation of China (No. 52371077), Natural Science Foundation of Hebei Province (No. E2022203026), European Union's Research and Innovation Program Horizon Europe under the Marie Skłodowska-Curie Actions grant agreement (No.101129996, SynAM), and UKRI Engineering and Physical Sciences Research Council.

Funding

This work was supported by National Natural Science Foundation of China, 10.13039/501100001809, 52371077.

Conflicts of Interest

The authors declare no conflicts of interest.

Data Availability Statement

The datasets used and/or analyzed during the current study are available from the corresponding author on reasonable request.

References

1. C. K. Cheng, L. B. Young, K. Y. Lin, et al., “Single- Crystal Hexagonal Perovskite YAlO3 Epitaxially on GaAs (111) A and (001) Using Atomic Layer Deposition,” *Microelectronic Engineering* 178 (2017): 125–127.
2. W. Q. Pei, X. H. Zhao, Y. X. Sun, et al., “Microstructure Evolution and Long- Term Oxidation Resistant Performance of Al_2O_3/Si_3N_4/ YAlO Composite Film,” *Journal of Alloys and Compounds* 1040 (2025): 183666.
3. K. K. Matsunouchi, N. Komatsu, C. H. Kimura, H. Aoki, and T. Sugino, “Growth and Properties of YAlO Film Synthesized by RF Magnetron Sputtering,” *Applied Surface Science* 255 (2009): 5021–5024.
4. A. Krasnikova, O. Lagutab, V. V. Lagutac, et al., “Photostimulated Creation of Election and Hole Centers in YAlO3:Mn: Thermoluminescence and Electron Paramagnetic Resonance Study,” Optical Materials 167 (2025): 117272.
5. J. W. Yang, J. Qiao, X. Y. Liu, et al., “Development of Duplex Stainless Steel Joints With Enhanced Strength and Ductility Using Magnetron- Sputtered TiN Crystal Coatings on Filler Wires in Laser Welding,” *Journal of Manufacturing Processes* 152 (2025): 816–832.
6. Yonenaga, T. Taishi, Y. Murao, and K. Inoue, “Growth of Tin- Doped Ge Crystals: A Comparison of Impurity Segregation Behavior With IV Element Crystals and Alloys,” *Journal of Crystal Growth* 676 (2026): 128452.

7. Kumar, S. P. Singh, and P. S. Son, "Elastic Properties of TiC and TiN Crystals in High Temperature Range," *Chemical Physics Impact* 8 (2024): 100617.
8. Y. Li, S. Q. Yang, L. G. Dong, J. Zhang, Z. Zheng, and J. Liu, "Effect of Crystal Orientation on the Nanoindentation Deformation Behavior of TiN Coating Based on Molecular Dynamics," *Surface & Coatings Technology* 467 (2023): 129721.
9. J. C. Bi, Z. Wang, W. Chen, et al., "Interfacial Coincidence Structure Between Rocksalt TiN and Perovskite Oxide YAlO 3 Studied at the Atomic Scale," *Physical Review B* 112, no. 16 (2025): 165407.
10. X. Y. Xu, C. Liu, Y. S. Hu, et al., "Epitaxial Growth and Band Energy Aligment of Ga_2O_3 Films on Diamond (001) Single Crystal Substrate," *Journal of Alloys and Compounds* 1020 (2025): 17955.
11. J. C. Zhang, H. Li, J. Huang, et al., "The Influence of Different Electron Transport Layers on the Hydrothermal Sb2S3 Quasi- Epitaxial Growth," *Thin Solid Films* 835 (2026): 140873.
12. J. C. Bi, R. Y. Zhang, S. Q. Peng, et al., "Robust Plasmonic Properties of Epitaxial TiN Films on Highly Lattice- Mismatched Complex Oxides," *Physical Review Materials* 5, no. 7 (2021): 15–19.
13. S. Peng, G. Li, J. Bi, et al., "Effect of Large Lattice Mismatch on Superconductivity and Plasmonic Properties of Epitaxial NbTiN Films," *ACS Applied Electronic Materials* 6, no. 4 (2024): 2544–2551.
14. S. Q. Peng, X. W. Wang, R. Y. Zhang, and M. Tang, "Reusability and Long- Life Storage SERS Substrate Based on Epitaxial Transition Metal Nitride Films With a Nanoisland- Like Surface," *Materials Letters* 390 (2025): 138414.
15. 15. Z. Wang, Q. H. Zhang, Y. W. Cao, et al., "Interfacial Coincidence Structure Between Rocksalt TiN and Perovskite Oxide $YAlO_3$, Studied at the Atomoic Scale," *Physical Review B* 112 (2025): 165407.
16. X. Z. Zhou, D. Y. Wang, T. P. Qu, et al., "An Approach to Heterointerfacial Engineering Based on the Long- Range Lattice Matching Model and Density Functional Theory," *Acta Materialia* 299 (2025): 12144.
17. G. Kresse and J. Hafner, "Ab initiomolecular dynamics for liquid metals," *Physical Review B* 47 (1993): 558–561.
18. G. H. Feng, S. Wang, A. Osman, et al., "4D Printing of Hierarchically Porous Carbon–Supported High- Entropy Ceramic Metamaterial for Tunable Microwave Absorption," *Science Advances* 12, no. 20 (2026): 0172.
19. J. P. Perdew, K. Burke, and M. Ernzerhof, "Generalized Gradient Approximation Made Simple," *Physical Review Letters* 77 (1996): 3865–3868.
20. G. H. Feng, L. X. Guo, H. Y. Yu, et al., "Uniting Superior Electromagnetic Wave Absorption With High Thermal Stability in Bioinspired Metamaterial by Direct Ink Writing," *Advanced Functional Materials* 35 (2025): 2424499.
21. D. Joubert, "From Ultrasoft Pseudopotentials to the Projector Augmented- Wave Method," *Physical Review B* 59 (1999): 1758–1775.
22. X. Yun, X. J. Ren, H. X. Zheng, et al., "Prediction of the Interfacial Relationship Between Y2O3 and TiN Using First- Principles Calculations," *Physical Chemistry Chemical Physics* 28 (2026): 8587.
23. B. L. Bramfitt, "The Effect of Carbide and Nitride Additions on the Heterogeneous Nucleation Behavior of Liquid Iron," *Metallurgical Transactions* 1 (1970): 1987–1995.

24. F. Chen, H. Jiang, and Y. Zhang, “First- Principles Calculation of Bonding and Hydrogen Trapping Mechanism of Fe3C/α- Fe Interface,” *Journal of Materials Research and Technology* 26 (2023): 6782–6793.
25. J. Wang, J. Yang, C. Wang, et al., “First- Principles Calculation on LaAlO3 as the Heterogeneous Nucleus of TiC,” *Computational Materials Science* 101 (2015): 108–114.

TABLE 1 | Mismatch degree of the low-index planes of $YAlO_3$ and TiN.

Matching plane	**$YAlO_3$(001)//TiN(100)**			**$YAlO_3$(001)//TiN(110)**		
$[uvw]_{YAlO_3}$	**[210]**	**[010]**	**[110]**	**[210]**	**[010]**	**[110]**
$[uvw]_{TiN}$	[011]	$[0\,\bar{1}\,1]$	[013]	$[1\,\bar{1}\,0]$	[001]	$[1\,\bar{1}\,1]$
θ (°)	0	0	3.435	0	0	5.264
d_{YAlO_3} (Å)	6.04	3.487	6.975	6.652	9.407	11.522
d_{TiN} (Å)	5.993	2.997	6.701	5.993	4.238	7.34
δ (%)		7.01			7.96	

TABLE 2 Surface energy of Y terminated surface model on $YAlO_3$ (001) plane (J/m^2).

Layer	**5**	**9**	**13**	**17**	**21**	**25**
$YAlO_3$(001)	2.11	2.1	2.08	2.07	2.06	2.06

TABLE 3 Surface energy of O1 terminated surface model on $YAlO_3$ (001) plane (J/m^2).

Layer	**7**	**11**	**15**	**19**	**23**	**27**	**31**
$YAlO_3$(001)	11.79	11.71	11.77	11.69	11.68	11.67	11.67

TABLE 4 Surface energy of O2 terminated surface model on $YAlO_3$ (001) plane (J/m^2).

Layer	**7**	**11**	**15**	**19**	**23**	**27**	**31**
$YAlO_3$(001)	−5.62	−5.89	−5.90	−5.90	−6.02	−6.05	−5.94

TABLE 5 Surface energy of AlO terminated surface model on $YAlO_3$ (001) plane (J/m^2).

Layer	**5**	**9**	**13**	**17**	**21**	**25**	**29**
$YAlO_3$(001)	10.82	10.8	10.79	10.78	10.76	10.75	10.74

TABLE 6 Surface energy of TiN(100) surface model (J/m^2).

Layer	**5**	**7**	**9**	**11**	**13**
TiN(100)	1.19	1.14	1.34	1.32	1.29

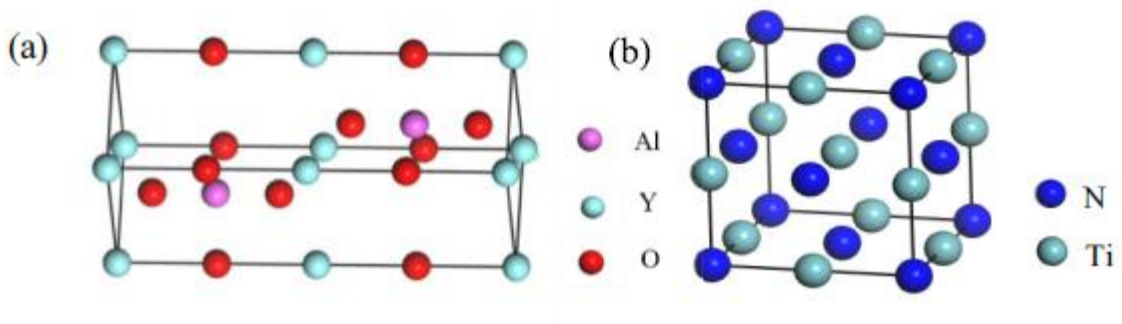

FIGURE 1 Crystal structures of $YAlO_3$ and TiN: (a) $YAlO_3$; (b) TiN.

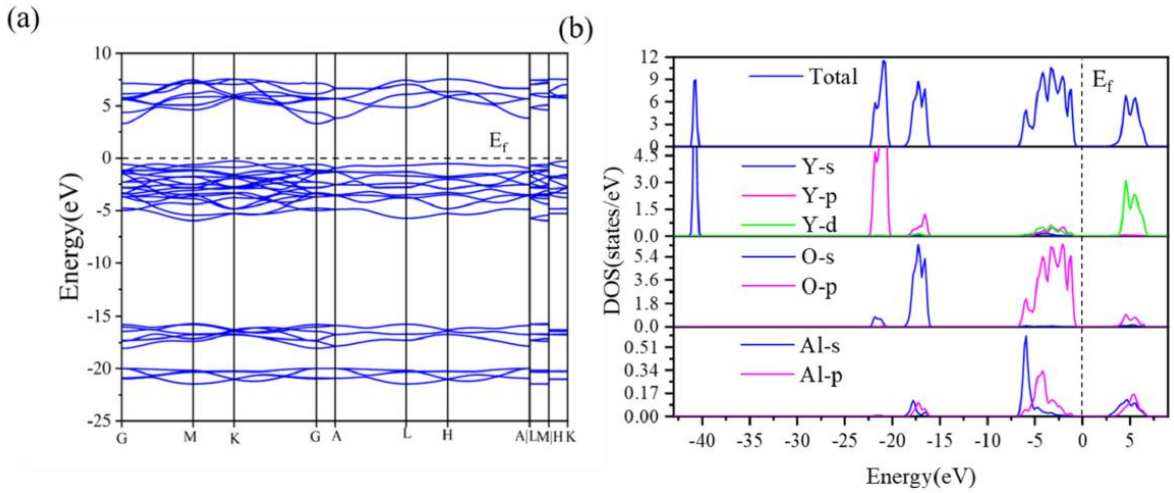

FIGURE 2 Bulk phase properties of $YAlO_3$: (a) energy band structure; (b) density of states diagram.

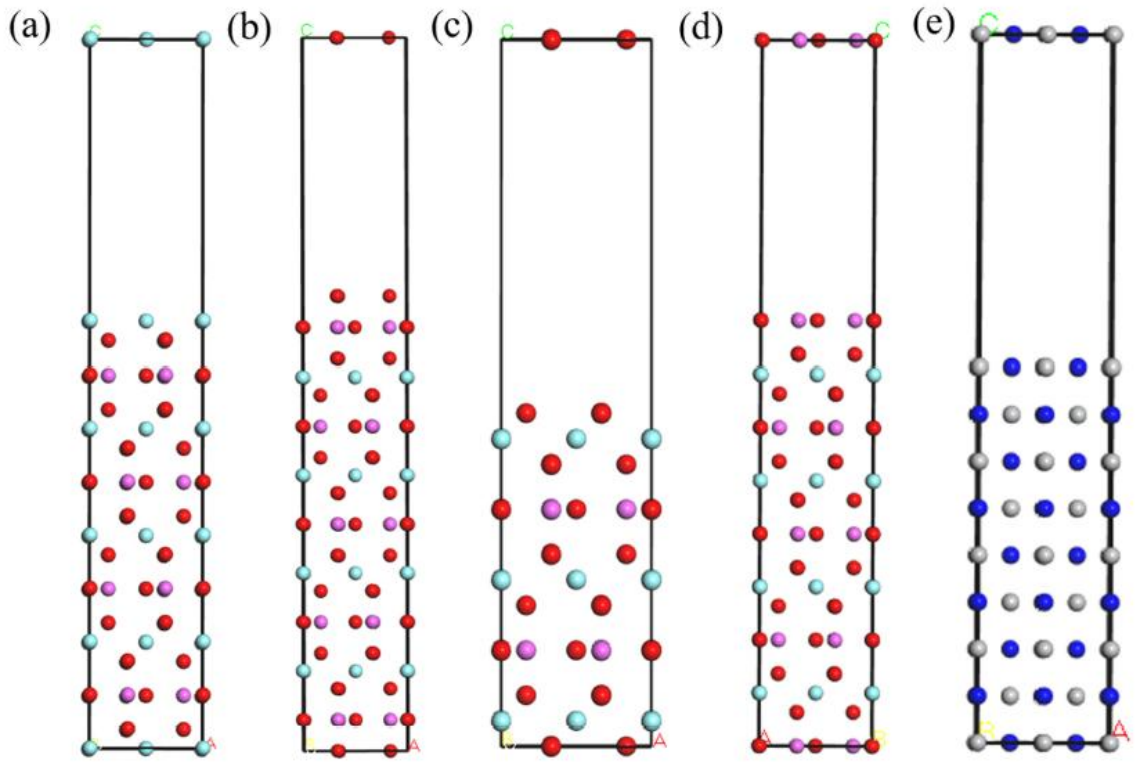

FIGURE 3 Surface models of $YAlO_3$ and TiN: (a) $YAlO_3$(001) with Y atom termination; (b) $YAlO_3$(001) with O1 atom termination; (c) $YAlO_3$(001) with O2 atom termination; (d) $YAlO_3$(001) with AlO atom termination; (e) TiN(100).

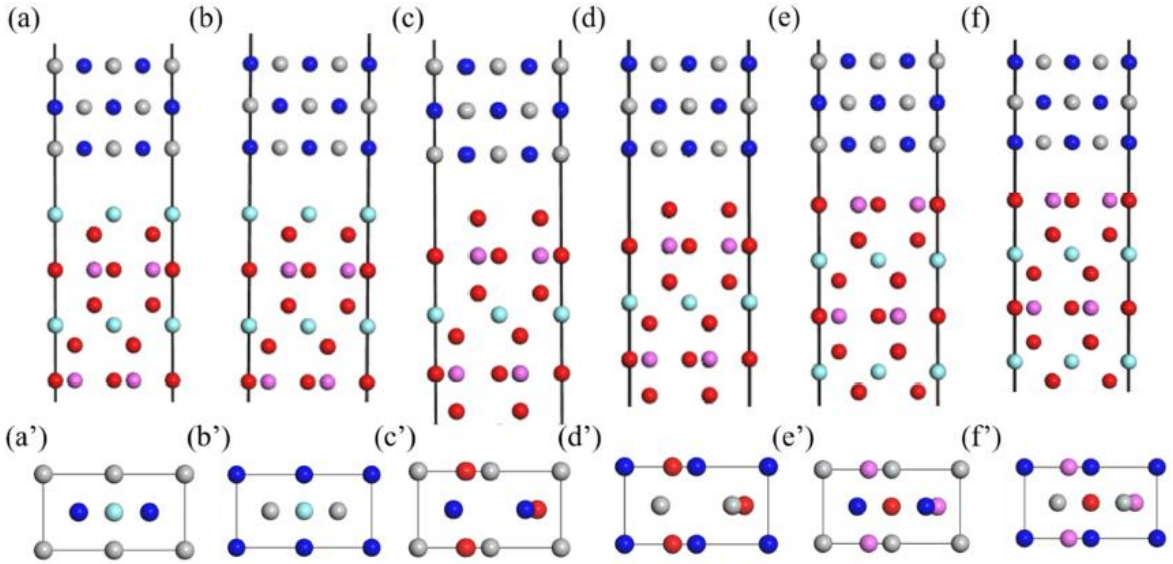

FIGURE 4 Six interface models of $YAlO_3$ and TiN interface: (a) Y-Ti; (b) Y-N; (c) O-Ti; (d) O-N;(e) AlO-Ti; (f) AlO-N.

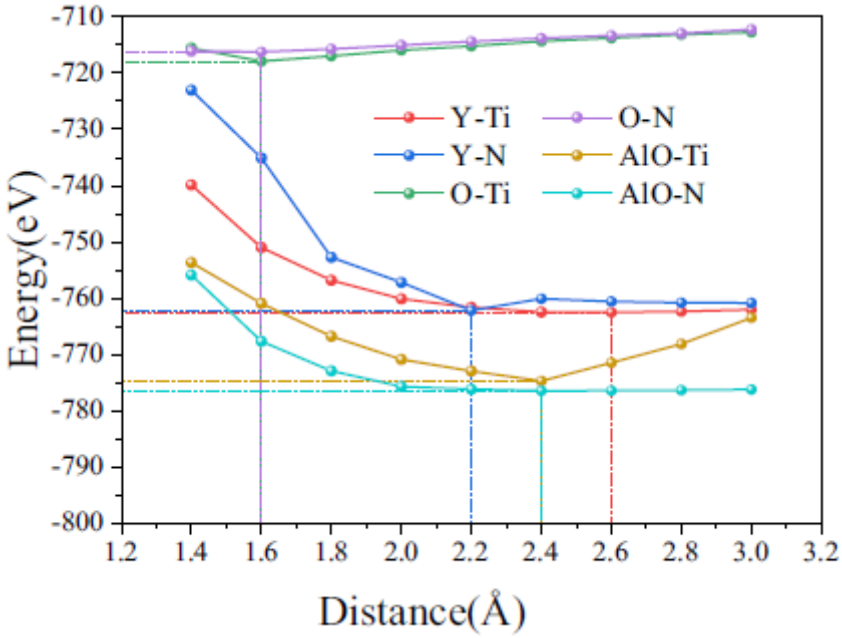

FIGURE 5 Energy variation diagrams of six $YAlO_3$ (001) and TiN100) interface models with respect to the interface spacing.

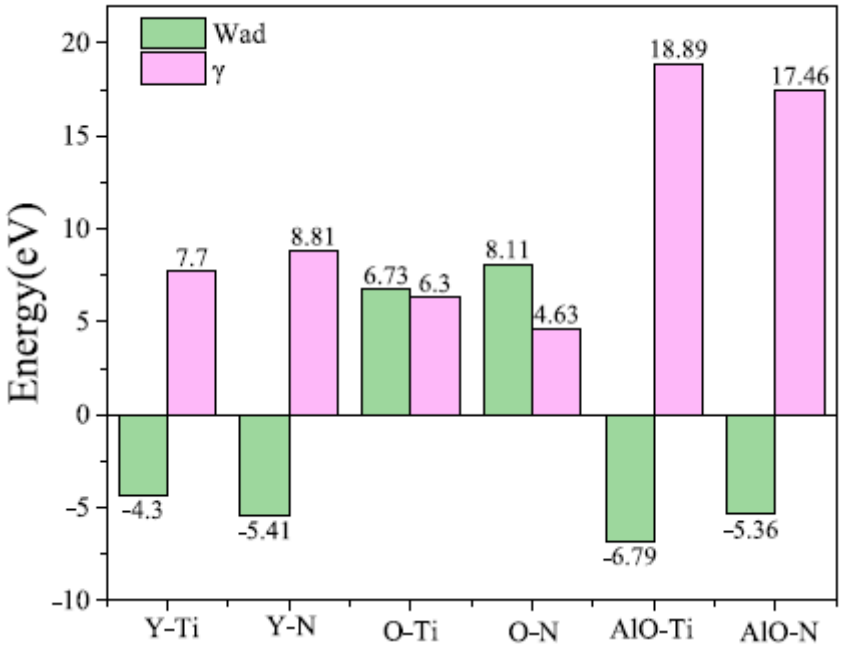

FIGURE 6 *Wad* and γ of six $YAlO_3$ (001) and TiN (100) interface models.

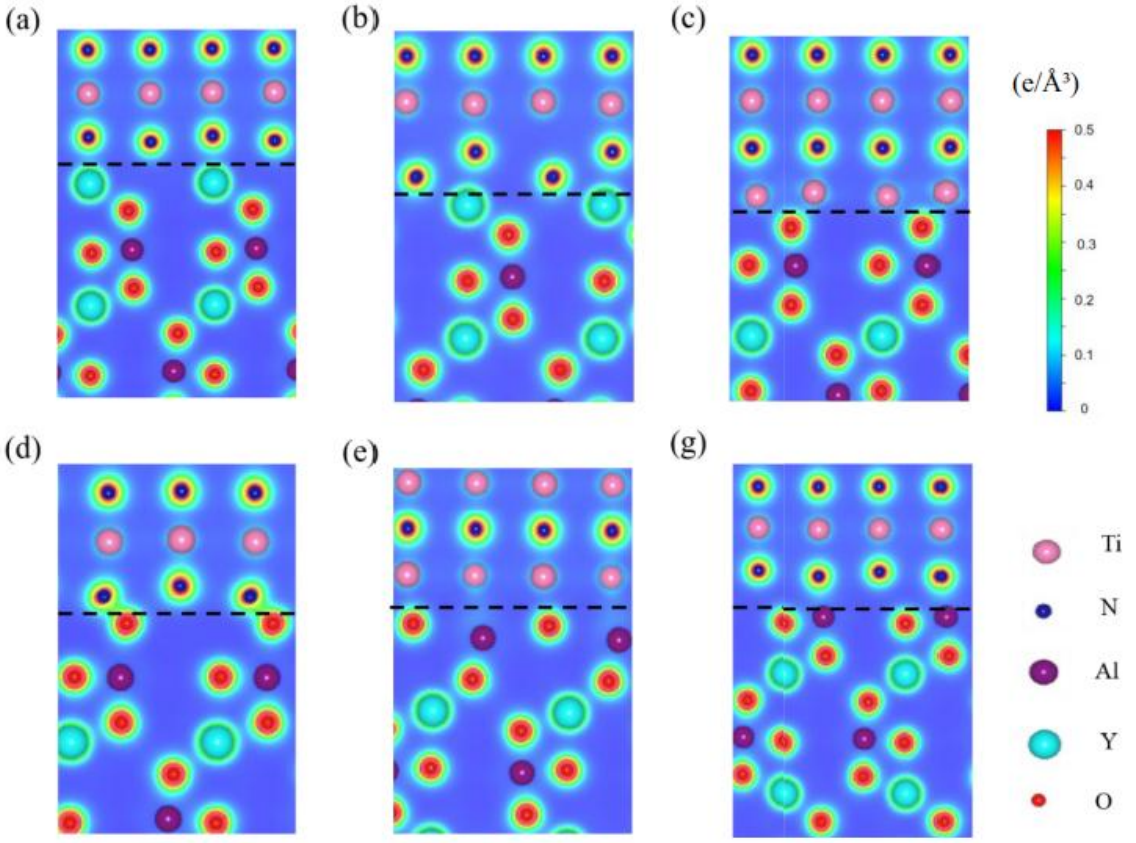

FIGURE 7 Charge density map of the (100) section of $YAlO_3$ (001) and TiN (100) interface models: (a) Y-Ti;(b) Y-N;(c) O-Ti;(d) O-N;(e) AlO-Ti;(f) AlO-N.

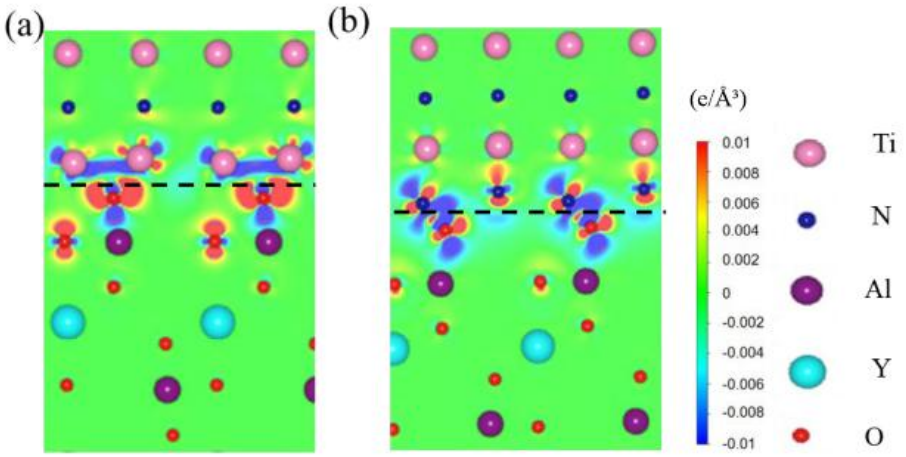

FIGURE 8 Differential charge density of the (100) section of $YAlO_3$ (001) and TiN (100) interface models: (a) O-Ti;(b) O-N.